Soft Matter

Accepted Manuscript

This is an *Accepted Manuscript*, which has been through the Royal Society of Chemistry peer review process and has been accepted for publication.

Accepted Manuscripts are published online shortly after acceptance, before technical editing, formatting and proof reading. Using this free service, authors can make their results available to the community, in citable form, before we publish the edited article. We will replace this *Accepted Manuscript* with the edited and formatted *Advance Article* as soon as it is available.

You can find more information about *Accepted Manuscripts* in the Information for Authors.

Please note that technical editing may introduce minor changes to the text and/or graphics, which may alter content. The journal's standard Terms & Conditions and the Ethical guidelines still apply. In no event shall the Royal Society of Chemistry be held responsible for any errors or omissions in this *Accepted Manuscript* or any consequences arising from the use of any information it contains.

ROYAL SOCIETY OF CHEMISTRY

www.rsc.org/softmatter

Dynamic Cassie-Baxter Model

Tingyi "Leo" Liu[*], *Zhiyu Chen*[†], *Chang-Jin "CJ" Kim*

Mechanical and Aerospace Engineering Department
University of California, Los Angeles (UCLA), California 90095, U.S.A .

ABSTRACT: Contact-angle hysteresis of a liquid suspended on surface microstructures, namely in a Cassie-Baxter state, is determined mainly by the receding contact line although not fully understood. Current modified Cassie-Baxter models predict some but not most experimental data in the literature. Noting that most models were based on two-dimensional (2-D) principle whereas the experiments were in three-dimensional (3-D) conditions, here we develop a 2-D experiment. While 3-D experiments measure the receding contact lines averaged over space and time, 2-D experiments eliminate the spatial averaging and can further eliminate the temporal averaging by high-speed visualization. The resulting details of the contact line motion lead us to propose a 2-D model, which incorporates the contact-line friction. The new 2-D model matches the 2-D experimental results excellently while all existing models show significant deviation. By introducing a line solid fraction term, the 2-D model is further generalized to a 3-D model, which successfully predicts a wide range of 3-D data in the literature regardless of their distinct microstructures and receding modes.

1. Introduction

Liquids suspended on micro- or nano-structured surfaces have attracted strong interests in recent years for their unusually large apparent contact angle and small contact angle hysteresis, i.e., the super-repellent (superhydrophobic for water) property. The Cassie-Baxter (CB) model[1] has long been used to describe the apparent contact angles of a suspended liquid with the solid and gas fraction, i.e., the areal proportion of the liquid-solid and liquid-vapor interfaces. Originally derived for the apparent advancing and receding contact angles[1], the CB model has been widely used for the apparent static contact angles assuming a thermodynamic equilibrium[2]. However, the original CB model was later found to be inaccurate for the apparent receding contact angles, leading to the probing studies in recent years[3–13]. Because contact angle hysteresis, i.e., the difference between the advancing and receding contact angles, is the main resistance to droplet movement on a surface and thus critical for many applications especially in small scales, e.g., droplet-based microfluidics[14,15], a model that accurately describes the advancing and receding contact angles is highly desired. Most often, the receding contact line

effectively controls the sliding dynamics of a CB droplet. This is because, unlike the large advancing angle (> 150°), which gives little room to vary[3–13,16] below 180°, the receding angle may vary significantly above 0°[12,17]. Since the CB equation fails to predict the receding contact angles on many of the today's superhydrophobic surfaces despite the importance, many have developed modified CB models[3–7,10,12,16].

Recent studies have shown the receding contact angle is mostly determined by the liquid-solid interaction close to the solid-liquid-vapor three-phase contact line (TCL)[3–6,16,18–20], leading to two main approaches of reflecting the contact-angle hysteresis in the CB theory. In one approach, the receding contact angles are calculated from local thermodynamic balance at the TCL instead of the entire area beneath the CB droplet[4,5,16]. In the other approach, the hysteresis is calculated from the locally (i.e., microscopically) deformed receding TCL, which creates a surface energy barrier against the TCL motion[6,7]. Although these approaches resulted in predictions matching their own experimental data and perhaps a few others in the literature, they lacked a *direct* comparison between theory and experiments needed.

Searching for a direct comparison and the insight it would bring about, we first note an inherent difference between existing models and the experiments, as follows. While the models were conceived on two-dimensional (2-D) configurations, the experimental data were obtained in three-dimensional (3-D) conditions[4–7,16]. No matter how the advancing and receding contact angles were measured, either by adding/subtracting a liquid [Figure 1(a)] or sliding a droplet on the surface [Figure 1(b)], there exists an inevitable mismatch between the apparent contact line of the usual droplet – which is continuous and circular – and the typical surface patterns that are isolated or linear, as illustrated in Figures 1(c) and (d). Such mismatch makes the measured contact angles affected by the neighboring contact angles along the TCL that are under different moving conditions. The mismatch could be avoided only if the contact line and the underlying pattern are aligned. One example is a spherical droplet on a circular surface pattern, as shown Figure 1(e), and another example is a rectangular droplet on a linear surface pattern, as shown in Figure 1(f). Although a 3-D model based on finite element method should have allowed a direct comparison with the experimental data obtained in 3-D, unfortunately discrepancies persisted between the simulated and experimental data[19].

Acknowledging the difficulty of 3-D, in this paper we propose an alternative approach of comparing 2-D models with 2-D experimental data. We first develop a new experimental apparatus[21] that resembles Figure 1(f) to generate and image the 2-D receding contact line motion. The 2-D measurement of apparent receding angles on a microstructured surface over a range of solid fractions allows us to directly compare the 2-D experimental data with the existing 2-D models in the literature. Since no existing model is found to explain the 2-D data, we develop a new model based on our observation of the 2-D contact line motion. Addition of a frictional term to the original CB equation results in a nice match with the 2-D data. Building on

the success, we then generalize the new model from 2-D to 3-D and find good agreements with the experimental data in the literature (i.e., 3-D data) across a wide range of surface structures and sliding conditions. The limitation of our model is also discussed.

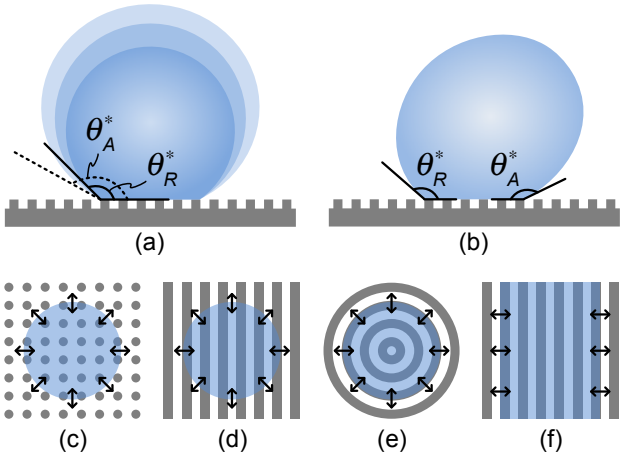

Figure 1. A CB droplet moving on a few exemplary structured surfaces, viewed from side (a,b) and top (c-f). (a) and (b) show the meniscus advancing and receding by adding and subtracting liquid to and from a droplet (a) and by translating a droplet on the surface (b). θ_A^* and θ_R^* represent the apparent advancing and receding contact angle, respectively. (c) and (d) show the contact line motions commonly employed to study dynamic contact angles in the literature. While the surface structures are in a linear pattern, the contact line sliding on them is circular, creating dynamic contact angles in 3-D conditions. (e) and (f) show the contact line motions allowing dynamic contact angles in 2-D conditions. (e) is a scenario of a spherical droplet on a concentric ring pattern. (f) is a scenario of a long cylindrical droplet traversing across parallel stripes, adopted for the current study.

2. Experiments

An apparent (or macroscopic, effective) contact angle θ^* is an angle seen far enough from the contact line so as not to be affected by the local (or microscopic, real, true, intrinsic, Young's) contact angles θ_Y and their variations right on the microstructures. When a meniscus slides across the microstructures so that the local TCL has to jump between them, the apparent contact angle would be a combination of local angles averaged in both space and time. To eliminate the average the local angles in space, we assessed the 2-D contact line motion from a virtual 2-D motion that resembles Figure 1(f) by traversing an elongated droplet on micro-gratings[21]. An elongated droplet is against the natural tendency of a liquid forming a sphere to minimize its surface, but we could shape a droplet using a wetting pattern on a solid surface[22,23].

As shown in Figure 2, a (hydrophobic) photoresist was coated and patterned on a glass plate to open a long, hydrophilic rectangle on which a droplet was confined as an axially truncated cylinder. The detailed fabrication process of each component can be found in the Supplementary Information. After careful alignment, the elongated water droplet attached to the top plate was put into contact with the superhydrophobic grating surface underneath. Held by the hydrophilic window on the top plate, the droplet formed advancing and receding meniscus on the superhydrophobic substrate, which slid parallel to the top plate (at a reasonable speed, e.g., ~0.5 mm/s, not to cause capillary instability or be affected by evaporation). Since the contact line traversing across the structures was the closest to a 2-D condition at the middle of the long droplet, the camera was focused at the middle plane of the elongated droplet. To resolve the local angles in time, on the other hand, the high-speed imaging was utilized at 6000 frames per second (fps), which captured the receding contact line motion in temporal details.

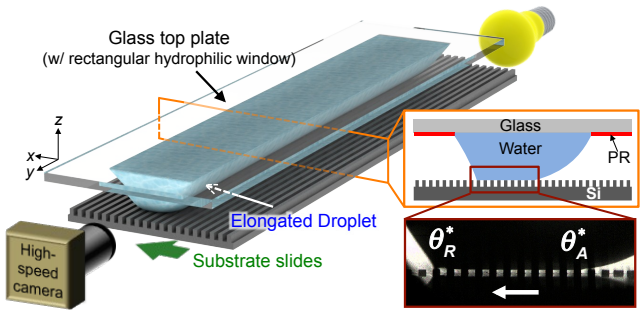

Figure 2. Apparatus to create and observe 2-D contact line motion. An elongated water droplet was formed via a long hydrophilic rectangle on a hydrophobic top plate and sandwiched on a superhydrophobic substrate of microgratings aligned to the rectangle. The cross-sectional views show the device configuration with a zoomed-in image captured during the experiment.

3. Results and Discussion

3.1 2-D receding contact line motion

For the 2-D experiments, grating structures of a fixed pitch of 200 μm with solid fraction ϕ_s (the ratio of the grating width to pitch) of 0.2, 0.3, 0.4, 0.5, 0.6, 0.7, and 0.8 were prepared and tested. Overall, the receding contact line periodically pinned on, slid on, and jumped across microstructures, presenting stick-slip motions consistent with observations from other researchers[8–11]. However, we were able to obtain far more details about the motion of the receding meniscus that would not have been possible without the 2-D condition and high-speed imaging. First, we were able to capture images of the receding meniscus that clearly showed two different contact angles depending on the measurement scale: (1) the local or microscopic receding contact angle measured right on the grating surfaces, and (2) the apparent or

macroscopic receding contact angle measured away from the grating surface – above by more than the length scale of the pitch, as shown in Figure 3. Second, we were able to capture the evolution of the meniscus on and above the surface as the contact line translated across the gratings that revealed the local and apparent contact angles over time and position. Using surface with ϕ_s = 0.5 as a specific example, Figure 4(a) shows the selected time-lapsed images of the meniscus translating to the right across the grating microstructures during one receding cycle. By defining 0.00 ms as the moment when the apparent contact angle equals the local contact angle, we can divide each cycle in to 4 stages: (1) TCL pins at the rear edge (i.e., left corner in the figure) of the microstructure; (2) TCL slides on the microstructure; (3) TCL jumps across microstructures (i.e., slides on air) to pin at the rear edge of the next microstructure; (4) with the TCL pinned, the meniscus relaxes while the local contact angle recovers the apparent receding angle. To better describe the detailed contact line behavior of each section, we introduce the mathematical analysis of the slopes at each point along the receding menisci[24]. The slope represents a spatial intermediate contact angle if one chooses to read the value at that intermediate height. By plotting those corresponding angles as a function of the distance (i.e., height) from the surface in Figure 4(b) and (c), the relations between the local and apparent contact angles are better illustrated.

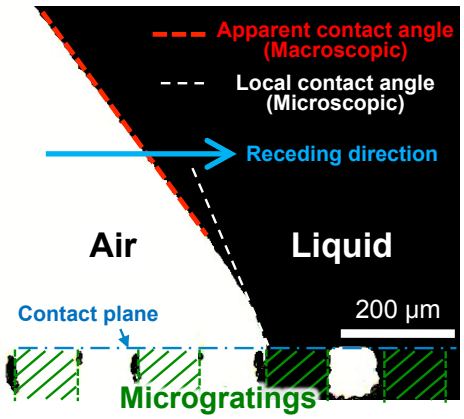

Figure 3. Apparent and local contact angles seen from a snapshot of the receding contact line during the 2-D experiment. The image has been converted into black and white for better contrast. Microstructures not in contact with the droplet are less visible due to the strong lighting from behind.

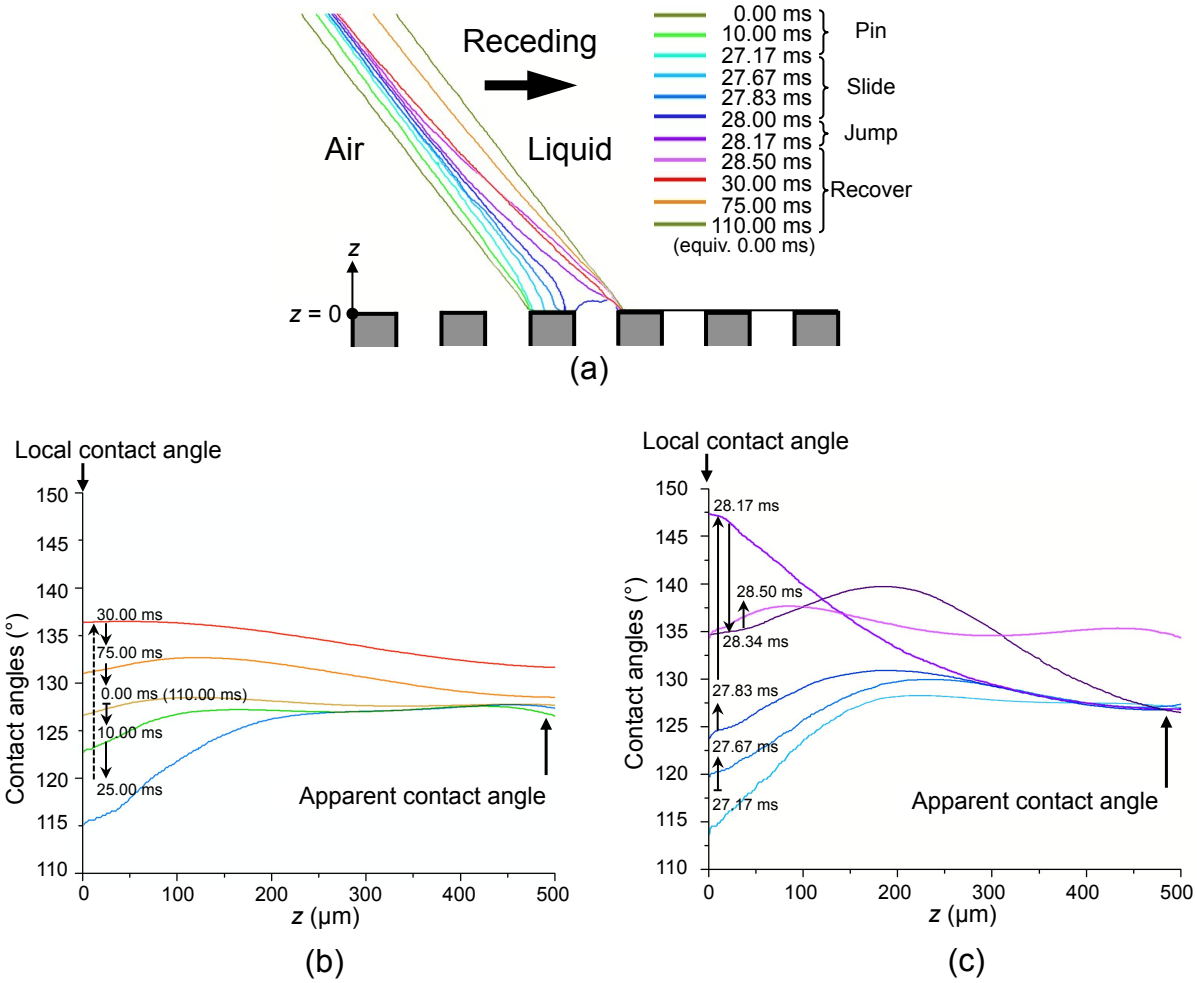

Figure 4. Evolution of the receding meniscus over one cycle of contact line translation across grating structures during 2-D experiment and detailed analysis of the corresponding contact angles. A Teflon®-coated micro-gratings with solid fraction $\phi_s = 0.5$ and pitch $P = 200$ μm was used for illustration. (a) Snapshots of the receding contact line overlapping in time sequence throughout one receding cycle. The meniscus lines were obtained from the high-speed images by edge detection using MATLAB software. The moment 0.00 ms was defined as the moment of local angle equaling the apparent angle. (b) Spatially intermediate contact angle versus height (z) measured over one receding cycle or 0.00-110.00 ms. (c) Spatially intermediate contact angle versus height (z) detailed over the dramatic period of receding contact line sliding and jumping from one structure to the next, i.e., stages 2 and 3 of receding or 27.17-28.50 ms.

Stage 1: TCL pins at the rear edge of the microstructure

As shown in Figure 4(a), the first stage ranged from 0.00 ms to 27.17 ms, starting with the local angle (meniscus slope at $z = 0$) aligned with the apparent receding angle (meniscus slope at $z = 500$ μm). During stage 1, because TCL was pinned, the local angle kept decreasing while the apparent angle remained at the receding value, as evidenced from the parallel menisci in Figure 4(a) and merging contact angles at $z > 400$ μm in Figure 4(b).

Stage 2 and 3: TCL slides and jumps on microstructure

At 27.17 ms, the local angle reached the receding contact angle of the smooth surface (i.e., 110° for Teflon®), prompting TCL to slide on the microstructure and jump across the microstructures within ~1 ms (i.e., from 27.17 ms to 28.17 ms). Figure 4(a) shows the meniscus staying nearly invariant away from the microstructures but deforming significantly near the microstructures in such a short period. Figure 4(c) illustrates the details of this dramatic period in terms of contact angles. While the apparent receding angle remained at ~126° away from the surface, the local contact angle jumped from ~110° to ~147° within mere 1 ms.

Stage 4: TCL recovers to receding state

After the TCL jumping, the suddenly increased local angle (~147° at 28.17 ms) started to propagate up along the meniscus as a capillary wave, forcing the apparent angle to increase from ~126° to ~135° in the next ~2 ms. Because the jumping made the TCL outpace the overall receding speed and the local angle became larger than the apparent receding angle, the TCL stopped receding while the top plate moved to catch up. Therefore, the TCL remained anchored to the rear edge of the microstructure until the local angle and the apparent angle became the same. However, this apparently long recovery period (from 28.17 ms to 110 ms) was an experimental artifact rather than an inherent phenomenon, as elaborated in Supplementary Information (Figure S2 and "*Influence of the top plate distance on the recovery of the apparent contact angle*"). In short, because the receding meniscus was pinned on the top plate, which was kept somewhat close to the bottom substrate to accommodate the elongated droplet in our 2-D experiment, the meniscus was stretched when the TCL jumped. In the true 2-D condition of Figure 1(f) with no or an infinitely distanced top plate, the apparent receding meniscus would not be stretched so that its angle, i.e., the apparent receding angle, would remain constant at all times.

3.2 2-D receding contact angles

For all tested surfaces with solid fraction ϕ_s between 0.2 and 0.8, the local receding contact angle on the Teflon®-coated microstructures (i.e., the microscopic angle below which the TCL starts to slide on their top surfaces) coincided with the receding contact angle on a smooth

Teflon® surface (i.e., θ_R = 110°) regardless of ϕ_s . In contrast, as shown in Figure 5, the apparent receding contact angle increased with decreasing solid fraction ϕ_s , following the trend generally found in the literature. However, the data deviated significantly from the predictions of all existing models[1,3,4,6,25] no matter which approach the model was based on, e.g., contact area based[1], contact line based[3,4], or deformed meniscus based[6]. Unlike the recent review[26], we do not find contact-line-based approach[3,4] more accurate than the other approaches. We interpret the discrepancy not surprising, since most of the models were derived assuming 2-D and tuned to match certain (mostly own) 3-D data in the absence of any 2-D data. While explaining the original CB model[1] in 2-D as commonly done today, the authors clearly understood the limitation of 2-D models in the 3-D world, as they specifically excluded 2-D conditions by stating that their model "is inapplicable when the wires (i.e., micro-gratings) are parallel" to the water meniscus "due to the water moving discontinuously" between microstructures[1], similar to Figure 1(f). Their model is valid only if the TCL does not completely align with the wires so that some parts of TCL slide on solid while the other parts slide on air. In our 2-D experiment, the discontinuous contact line motion, i.e., TCL jumping detailed in Figure 4(c), turned out to be a distinctive nature of the 2-D receding, urging us to develop a model adequately describing the observed phenomena.

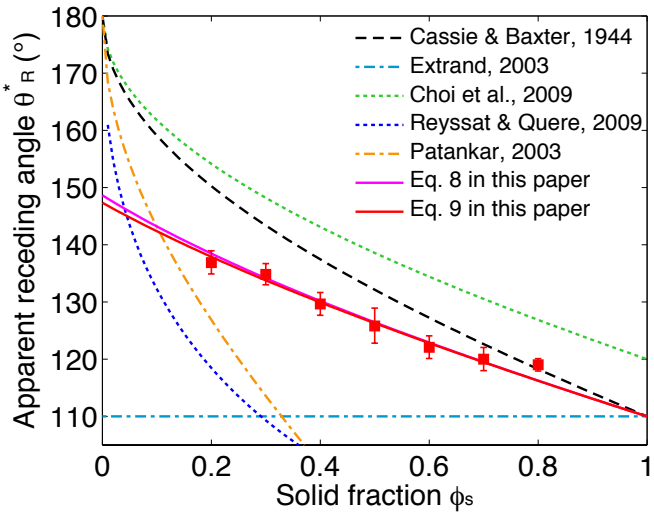

Figure 5. The 2-D apparent receding contact angles measured on the grating surfaces (shown as red solid squares with error bars) are compared with various models (shown as lines). The 2-D model in this paper (solid lines) was the only one that fit the 2-D experimental data; all other models in the literature (broken lines) deviated from the 2-D data significantly. From a same model, Eq. 8 and Eq. 9 represent the theoretical upper and lower bound of the apparent receding angles. For all the models, θ_Y = 120° and θ_R = 110° (measured from a Teflon®-coated smooth surface) were used to calculate θ_R^*.

4. Theoretical Modeling for 2-D Receding

To model the apparent receding angle on microstructured surface, we first revisit the receding on a smooth surface and then introduce the solid fraction effect of the microstructured surface with the information about the contact line motion observed in our experiments. As shown in Figure 6(a), the angle of contact at equilibrium on an ideal surface (smooth, homogeneous, and rigid) can be given by the Young's equation[27]:

$$\gamma_{SV} = \gamma_{SL} + \gamma \cos\theta_Y \tag{1}$$

where γ_{SV} and γ_{SL} are the surface tension at the solid-vapor and solid-liquid interface, respectively. In reality, the contact angle of a sliding meniscus is different from the Young's angle. We quantify such difference by a friction force f acting on the TCL, as was proposed in 1920s[28] and found in good agreement with experimental data[29,30]. Therefore, on a receding meniscus depicted in Figure 6(b), we have the force balance as,

$$\gamma_{SV} + f_R = \gamma_{SL} + \gamma \cos\theta_R \tag{2}$$

where θ_R θ_R is the local receding contact angle and f_R is the receding line friction, which can be calculated from Eqs. 1 and 2 as:

$$f_R/\gamma = \cos\theta_R - \cos\theta_Y \tag{3}$$

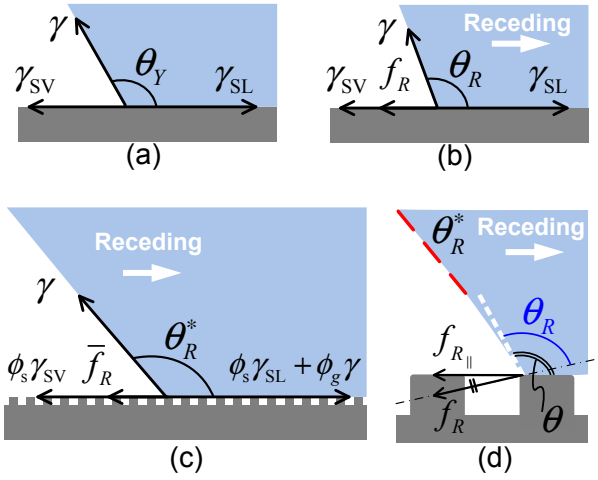

Figure 6. Force balances at contact lines on smooth and structured surfaces. (a) Young's relation describes the balance in equilibrium for an ideal surface without hysteresis. (b) Forces balance at the receding contact line on a smooth surface by introducing line friction f_R to represent the contact angle hysteresis. (c) Forces balance at the apparent receding contact line on a structured surface of infinitely long ridges. Only macroscopic forces are considered in this picture showing apparent contact angle. (d) Microscopic analysis of the contact line resistance when the contact

line is pinned at he rear edge of the microstructure, showing both local and apparent contact angles.

Now, let us examine a meniscus receding on an infinitely long periodic gratings [i.e., true 2-D of Figure 1(f)] with solid fraction ϕ_s and gas fraction ϕ_g , i.e., ϕ_s = (liquid-solid interface)/(pitch) and ϕ_g = (liquid-vapor interface)/(pitch). During 2-D receding, as shown in Figure 6(c), macroscopically the contributions of solid-vapor and solid-liquid interfacial tensions on microstructures can be revised as $\gamma'_{\mathrm{SV}} = \phi_s \gamma_{\mathrm{SV}}$ and $\gamma'_{\mathrm{SL}} = \phi_s \gamma_{\mathrm{SL}} + \phi_g \gamma$ while liquid surface tension remains as γ . The force balance at the apparent receding TCL can be written as

$$\phi_s \gamma_{\mathrm{SV}} + \overline{f}_R = \phi_s \gamma_{\mathrm{SL}} + \phi_g \gamma + \gamma \cos\theta_R^* \tag{4}$$

where $\overline{f}_R$ is the equivalent resistant force acting on the apparent receding TCL. Using the impulse theory, $\overline{f}_R$ can be calculated by averaging resistant force in the lateral direction ($f_{R_\parallel}$) over one receding cycle T, i.e., $\overline{f}_R = \left(1/T\right)\int_0^T f_{R_\parallel}\left(t\right)dt$, where T consists of the time TCL pins on (T_p), slides on (T_s), and jumps across (T_j) microstructures, i.e., $T = T_p + T_s + T_j$. We note again that if there were no top plate that would constrain the meniscus movement in our experiment, the apparent angle would have remained the same all the time, i.e., stage 4 observed in our experiment does not exist in a true 2-D condition as explained in Figure S2. According to our experimental observation on micro-gratings with $\phi_s = 0.5$, the time of TCL pinning (i.e., 0-27.17 ms in 28.17 ms, viz., ~96.5% of time) dominated over the time of TCL sliding (i.e., 27.17-28.00 ms in 28.17 ms, viz., ~2.9% of time) and TCL jumping (i.e., 28.00-28.17 ms in 28.17 ms, viz., ~0.6% of time). Therefore, $\overline{f}_R$ can be approximated by the resistance during contact line pinning and can be calculated from the local force balance shown in Figure 6(d) as

$$\overline{f}_R \approx \frac{1}{T_p}\int_0^{T_p} f_{R_\parallel}\left(t\right)dt = \frac{1}{\left|\theta_R - \theta_R^*\right|}\int_{\theta_R^*}^{\theta_R} f_R \cos\left(\theta - \theta_R\right)d\theta \tag{5}$$

where θ is the local contact angle. We also assumed a constant angular velocity when the meniscus curves around the edges of individual microstructures, considering mathematically differentiable (i.e., not ideally sharp) corners, so that local receding angle can be formed along the edges. Integrating Eq. 5 and expanding it in the Taylor series yields

$$\overline{f}_R \approx f_R \cdot \sum_{k=1}^{\infty} \frac{\left(-1\right)^{k-1}\left(\theta_R^* - \theta_R\right)^{2k-2}}{\left(2k-1\right)!} = f_R \cdot \left[1 - \frac{\left(\theta_R^* - \theta_R\right)^2}{6} + \frac{\left(\theta_R^* - \theta_R\right)^4}{120} - \ldots\ldots\right] \tag{6}$$

Since the above Taylor series converges, the first two terms define the upper and lower limit of $\overline{f}_R$. Higher order terms will be neglected from the discussion below. Utilizing the CB model[2] for the apparent static contact angle θ^* as

$$\cos\theta^* = \phi_s \cos\theta_Y - \phi_g \tag{7}$$

and combining Eq. 7 with Eqs. 1-4 and 6 to eliminate γ_{SV}, γ_{SL}, and f_R, we obtain a modified CB equation for a 2-D receding meniscus:

$$\cos\theta_R^* = \cos\theta^* + \left(\cos\theta_R - \cos\theta_Y\right)\left[1 - \left(\theta_R^* - \theta_R\right)^2 / 6\right] \tag{8}$$

Equation 8 is a transcendental equation that is difficult to use because it can only be solved numerically. However, if the second term in the bracket turns out much smaller than the first term, i.e., $\left(\theta_R^* - \theta_R\right)^2 / 6 \ll 1$, Eq. 8 can be approximated as

$$\cos\theta_R^* = \cos\theta^* + \left(\cos\theta_R - \cos\theta_Y\right) \tag{9}$$

The use of Eq. 9 over Eq. 8 is reasonable as long as the difference between apparent and local angle is small (e.g., ~45° for 10% error) as for our case. This is confirmed in Figure 5 that both Eq. 8 and Eq. 9 fit the 2-D data very well and they branch only at very small ϕ_s when difference between θ_R^* and θ_R becomes large. All the 2-D data matched our model except for ϕ_s = 0.8. We speculate that the slight mismatch at ϕ_s = 0.8 was caused by a poor alignment of the rectangular hydrophilic window on the top plate with the micro-gratings on the substrate, because the visual alignment was exceedingly difficult when ϕ_s was large and the field was dark. As a result, the experiment of ϕ_s = 0.8 likely have resembled a 3-D sliding case considered by Cassie and Baxter[1] and thus matched the original CB model (black dashed line in Figure 5). This kind of 3-D sliding can be easily included in our model generalized for 3-D, as shown in the next section. Although the derivation in this section is based on force analysis, in principle one should be able to obtain the same result from thermodynamic energy balance if the energy stored in a curved meniscus (i.e., local contact angle) and its dissipation (through viscous loss during capillary wave created when the meniscus jumps) is properly accounted for.

5. Model Generalization for 3-D Receding

The 2-D model established above matched our 2-D data, which could not be predicted by any existing models in the literature developed to fit 3-D data. The question now is whether our model (Eq. 9), developed to fit 2-D data, can be generalized to predict 3-D data. To do so, we examine the two terms that contributed to θ_R^* in Eq. 9. The first term θ^*, which is the static apparent contact angle term calculated from the CB equation, considers only the solid fraction

and is therefore applicable to 3-D conditions. However, the second term $\left(\cos\theta_R - \cos\theta_Y\right)$, which is the hysteresis effect originated from the line friction f_R, should be modified to account for the receding conditions in 3-D. For example, for isolated structures (e.g., gratings and posts) the resistance against meniscus sliding comes from discrete solid structures but little from the air in between. In this case, the receding meniscus experiences only a fraction of the resistance compared to the 2-D condition, where the entire TCL is on solid structures. Because f_R exerts solely on the TCL in the direction opposite to the movement, the net resistance should be calculated as the sum (i.e., line integral) of f_R along the entire length of the real TCL. Therefore, we modify our model (Eq. 9) to accommodate receding TCL in 3-D conditions:

$$\cos\theta_R^* = \cos\theta^* + \left(\cos\theta_R - \cos\theta_Y\right)\lambda_s \tag{10}$$

where λ_s is defined as the line solid fraction, or the length ratio of real TCL to the apparent TCL for a receding TCL, as elaborated in Figure S3 in a manner analogous to the areal solid fraction ϕ_s defined in Reference 1. Particularly, Eq. 10 reduces to Eq. 9, if the surface structures are micro-gratings (i.e., stripes) and slides under 2-D condition, i.e., λ_s = 1, as our 2-D experiment. In contrast, when the TCL was sliding on micro-gratings but at certain angle (i.e., 3-D condition investigated by Cassie and Baxter[1]), we find a simple geometrical similarity leads to $\lambda_s = \phi_s$ and Eq. 10 reduces to the original CB model for receding[1]. We note that, although λ_s in Eq. 10 may appear similar to the semi-empirical parameters commonly proposed in the literature[3,11,31], λ_s is fully analytical. Instead, λ_s depends not only on the structure geometries but also on the receding conditions (e.g., direction), as illustrated in Figure S4. For example, for microstructures of an asymmetric geometry (e.g., triangular posts), λ_s may depend on the direction of receding[32]. For a given 3-D condition, λ_s needs to be calculated to obtain a spatial average along the apparent TCL over the segment of interest (see "*Definition and calculation of line solid fraction*" in the Supplementary Information). With the above recognition, we examined Eq. 10 against the experimental (3-D, needless to say) data of receding contact angles in the literature[1,7,12,13,19,31] by calculating λ_s for each corresponding case (Table S1), and found consistently good agreements, as summarized in Figure 7. Similarly to Figure 5, each set of data is compared with existing modified CB models in Figure S5.

For connected structures such as holes, unlike the cases of isolated structures discussed so far, TCL cannot be fully destabilized and remains pinned because the surface continues around the holes. Such TCL pinning across the holes[3,12] produces additional resistance against meniscus sliding. To account for all resistances, we further generalize Eq. 10 into a summation form:

$$\cos\theta_R^* = \cos\theta^* + \sum_i \left(\cos\theta_{R_i} - \cos\theta_{Y_i}\right)\lambda_{s_i} \tag{11}$$

where *i* denotes a specific kind of resistance. Figure 7 also includes the two sets of experimental data on hole structures reported by Priest et al.[12] and the predictions made by Eq. 11 with λ_s calculated for each case (Table S1). The fewer and more scattered data from hole structures compared with those from posts are probably caused by the difficulties in measurement (e.g., more sensitive to fabrication defects due to connected structures). Since Eq. 11 includes all the resistances in the summation without specifying or limiting the types of material, we further note the equation should be valid for chemically heterogeneous surfaces as well.

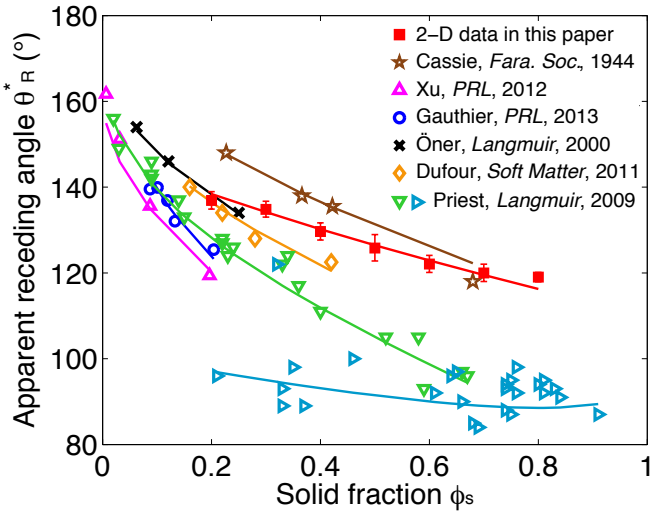

Figure 7. The measured data on the various surfaces in the literature (colored hollow symbols) are compared with the predictions by the generalized CB model (Eq. 10) using an appropriate λ_s for each case (correspondingly colored lines). The 2-D experimental data (red solid squares) are also compared with the prediction Eq. 10 using λ_s = 1 (red line), which is equivalent to Eq. 9. The conditions of receding on the structures are summarized in Table S1. Despite the wide range of variations in surface structures and receding conditions, Eq. 10 successfully describes all the experimental data.

Unlike the well-organized microstructures used for the scientific studies[1,7,12,13,19,31], the roughness found in nature and industrial applications are normally of random pattern and two-tier in micro- and nanoscale. Noting the summation nature of Eq. 11, we suggest the possibility of the model further generalized for random roughness by, for example, first 3-D mapping and decomposing the roughness into multiple simple patterns (such as gratings and posts) and then calculating and superposing their respective resistance contributions.

Lastly, we would like to discuss the limitation of our model. As shown through our derivation, the use of Eq. 9 (instead of Eq. 8) required that the apparent receding angle θ_R^* be not too much larger than the local receding angle θ_R or solid fraction be not too small; otherwise the second order term in Eq. 8 would deviate from being negligible. For example, Eq. 10, which is based on Eq. 9, is not likely to give an accurate estimation for wetting liquids (i.e., organic solvents) suspended on structured surfaces (i.e., superoleophobic surfaces), where the local receding angle is much smaller than 90° while the apparent receding may be much larger than 90°[4,33]. This shortcoming of Eqs. 9 and 10 originates from the fact that our model is built on experimental observation where water meniscus cleanly detached from hydrophobic microstructures before jumping to the next. On super-repellent surfaces made of hydrophilic materials, in contrast, the meniscus is known to be pinched off before jumping[34,35] – a phenomenon not accounted for in our current model. To investigate such an unusual case, one would need a repellent surface made of hydrophilic microstructures with unambiguous liquid-solid fraction[33] and the ability to measure the local angle at pinching-off on the microstructures.

6. Conclusions

We have performed a novel experiment to capture and reveal the 2-D receding contact line motion instead of the universally observed 3-D condition. Based on the new insight into the contact-line dynamics over microstructures through the 2-D experiment, we have developed a modified CB model including the frictional effect at the contact line and found good agreement with our measured 2-D apparent receding contact angles whereas all existing models deviated significantly. By introducing a line solid fraction in analogy to the areal solid fraction of the CB model, we have further developed a generalized CB model that satisfies 3-D conditions and showed consistently good agreements with the wide range of data in the literature.

ACKNOWLEDGMENT

This work has been supported by the NSF Grant (No. 1336966).

Supplementary Information. It contains details of device fabrication, expanded discussion of the dynamic contact angle measurements, definition and calculation of the line solid fraction λ_s and comparison of 3-D data to existing models.

Corresponding Author

*E-mail: leolty@ucla.edu; Tel 1-310-825-3977; Fax 1-310-206-2302.

Present Addresses

† Mr. Zhiyu Chen is currently with LinkedIn Corporation, Cupertino, CA, 95014.

REFERENCES

1. A. Cassie and S. Baxter, "Wettability of porous surfaces," *Trans. Faraday Soc.*, 1944, **40**, 546–551.
2. R. E. Johnson and R. H. Dettre, in *Contact Angle, Wettability, and Adhesion*, American Chemical Society, 1964, vol. 43, pp. 112–135.
3. C. W. Extrand, "Model for contact angles and hysteresis on rough and ultraphobic surfaces," *Langmuir*, 2002, **18**, 7991–7999.
4. W. Choi, A. Tuteja, J. M. Mabry, R. E. Cohen, and G. H. McKinley, "A modified Cassie-Baxter relationship to explain contact angle hysteresis and anisotropy on non-wetting textured surfaces," *J. Colloid Interface Sci.*, 2009, **339**, 208–216.
5. R. Raj, R. Enright, Y. Zhu, S. Adera, and E. N. Wang, "Unified Model for Contact Angle Hysteresis on Heterogeneous and Superhydrophobic Surfaces," *Langmuir*, 2012, **28**, 15777–15788.
6. M. Reyssat and D. Quéré, "Contact Angle Hysteresis Generated by Strong Dilute Defects," *J. Phys. Chem. B*, 2009, **113**, 3906–3909.
7. R. Dufour, M. Harnois, V. Thomy, R. Boukherroub, and V. Senez, "Contact angle hysteresis origins: investigation on super-omniphobic surfaces," *Soft Matter*, 2011, **7**, 9380–9387.
8. R. Dufour, M. Harnois, Y. Coffinier, V. Thomy, R. Boukherroub, and V. Senez, "Engineering sticky superomniphobic surfaces on transparent and flexible PDMS substrate," *Langmuir*, 2010, **26**, 17242–17247.
9. C. Dorrer and J. Rühe, "Advancing and receding motion of droplets on ultrahydrophobic post surfaces," *Langmuir*, 2006, **22**, 7652–7657.
10. A. Shastry, S. Abbasi, A. Epilepsia, and K.-F. Bohringer, in *International Solid-State Sensors, Actuators and Microsystems Conference (Transducers'07)*, 2007, pp. 599–602.
11. A. T. Paxson and K. K. Varanasi, "Self-similarity of contact line depinning from textured surfaces," *Nat. Commun.*, 2013, **4**, 1492.
12. C. Priest, T. W. Albrecht, R. Sedev, and J. Ralston, "Asymmetric wetting hysteresis on hydrophobic microstructured surfaces," *Langmuir*, 2009, **25**, 5655–5660.
13. D. Öner and T. J. McCarthy, "Ultrahydrophobic surfaces. Effects of topography length scales on wettability," *Langmuir*, 2000, **16**, 7777–7782.
14. W. C. Nelson and C.-J. Kim, "Droplet Actuation by Electrowetting-on-Dielectric (EWOD): A Review," *J. Adhes. Sci. Technol.*, 2012, **26**, 1747–1771.
15. S. Sharma, M. Srisa-Art, S. Scott, A. Asthana, and A. Cass, in *Microfluidic Diagnostics*, eds. G. Jenkins and C. D. Mansfield, Humana Press, Totowa, NJ, 2013, vol. 949, pp. 207–230.
16. S. T. Larsen and R. Taboryski, "A Cassie-like law using triple phase boundary line fractions for faceted droplets on chemically heterogeneous surfaces," *Langmuir*, 2009, **25**, 1282–1284.

17. W. Chen, A. Y. Fadeev, M. C. Hsieh, D. Öner, J. Youngblood, and T. J. McCarthy, "Ultrahydrophobic and Ultralyophobic Surfaces: Some Comments and Examples," *Langmuir*, 1999, **15**, 3395–3399.
18. J. F. Joanny and P.-G. de Gennes, "A model for contact angle hysteresis," *J. Chem. Phys.*, 1984, **81**, 552–562.
19. A. Gauthier, M. Rivetti, J. Teisseire, and E. Barthel, "Role of kinks in the dynamics of contact lines receding on superhydrophobic surfaces," *Phys. Rev. Lett.*, 2013, **110**, 046101.
20. L. Gao and T. J. McCarthy, "Wetting 101°," *Langmuir*, 2009, **25**, 14105–14115.
21. Z. Chen and C.-J. Kim, in *Proc. Int. Conf. Miniaturized Systems for Chemistry and Life Sciences (μTAS)*, Jeju, Korea, 2009, pp. 1362–1364.
22. B. Zhao, J. S. Moore, and D. J. Beebe, "Surface-directed liquid flow inside microchannels," *Science*, 2001, **291**, 1023–1026.
23. G. Sun, T. Liu, P. Sen, W. Shen, C. Gudeman, and C.-J. Kim, "Electrostatic Side-Drive Rotary Stage on Liquid-Ring Bearing," *J. Microelectromechanical Syst.*, 2014, **23**, 147–156.
24. Z. Chen, M.S. thesis, University of California, Los Angeles, 2009.
25. N. A. Patankar, "On the modeling of hydrophobic contact angles on rough surfaces," *Langmuir*, 2003, **19**, 1249–1253.
26. H. Y. Erbil, "The debate on the dependence of apparent contact angles on drop contact area or three-phase contact line: A review," *Surf. Sci. Rep.*, 2014, **69**, 325–365.
27. T. Young, "An Essay on the Cohesion of Fluids," *Philos. Trans. R. Soc. Lond.*, 1805, **95**, 65–87.
28. N. K. Adam and G. Jessop, "Angles of contact and polarity of solid surfaces," *J. Chem. Soc. Trans.*, 1925, **127**, 1863–1868.
29. X. D. Wang, X. F. Peng, J. F. Lu, T. Liu, and B. X. Wang, "Contact angle hysteresis on rough solid surfaces," *Heat Transfer—Asian Res.*, 2004, **33**, 201–210.
30. M. J. Santos and J. A. White, "Theory and simulation of angular hysteresis on planar surfaces," *Langmuir*, 2011, **27**, 14868–14875.
31. W. Xu and C.-H. Choi, "From sticky to slippery droplets: dynamics of contact line depinning on superhydrophobic surfaces," *Phys. Rev. Lett.*, 2012, **109**, 024504.
32. A. Nakajima, Y. Nakagawa, T. Furuta, M. Sakai, T. Isobe, and S. Matsushita, "Sliding of Water Droplets on Smooth Hydrophobic Silane Coatings with Regular Triangle Hydrophilic Regions," *Langmuir*, 2013, **29**, 9269–9275.
33. T. Liu and C.-J. Kim, "Turning a surface superrepellent even to completely wetting liquids," *Science*, 2014, **346**, 1096–1100.
34. R. Dufour, P. Brunet, M. Harnois, R. Boukherroub, V. Thomy, and V. Senez, "Zipping effect on omniphobic surfaces for controlled deposition of minute amounts of fluid or colloids," *Small*, 2012, **8**, 1229–1236.
35. J. W. Krumpfer, P. Bian, P. Zheng, L. Gao, and T. J. McCarthy, "Contact angle hysteresis on superhydrophobic surfaces: an ionic liquid probe fluid offers mechanistic insight," *Langmuir*, 2011, **27**, 2166–2169.

GRAPHICAL ABSTRACT